A REGULARIZED FILTERING APPROACH TO 2D DECONVOLUTION OF PRESTACK DEPTH MIGRATED SEISMIC IMAGES WITH THE USE OF RESOLUTION FUNCTIONS

A.K. Takahata, L.-J. Gelius, R.R. Lopes, I. Lecomte and M. Tygel

email: *kazuo@decom.fee.unicamp.br*
keywords: *seismic imaging, resolution, 2D deconvolution*

ABSTRACT

The distortion effects on pre-stack depth migrated (PSDM) images caused by limitations in acquisition geometry and frequency bandwidth can be modelled as the 2D convolution between the actual response and a resolution function. In the case of Born scattering, the resolution function describes the point spread function (PSF). These PSFs can be calculated with relatively low computational effort by the ray tracing technique. In this paper, we first review the basic idea of the PSF, its relationship with seismic images generated by PSDM, followed by its estimation. Next, we propose the use of 2D spiking deconvolution with the aim of minimizing these image distortions. Finally, the potential and limitations of the proposed method are explored with applications on controlled synthetic data.

INTRODUCTION

The concept of resolution function has been adopted in works such as Lecomte and Gelius (1998), Gelius and Lecomte (2000) and Gelius et al. (2002) in order to quantify the distortion of pre-stack depth migrated (PSDM) images caused by limitations in acquisition geometry and frequency bandwidth. As advocated in Gelius and Lecomte (2000), if Born scattering is assumed, the resolution function describes the so called *point spread function* (PSF). The concept of PSFs has been used widely in the image processing community in order to quantify the amount of image degradation caused by blurring (for a complete review, see, for example, Banham and Katsaggelos, 1997). An interesting application is the deblurring of images produced by the Hubble Space Telescope found in Lecomte (2008). Within seismic processing, a PSDM image can be modelled as the convolution between the PSF and the actual model quantities (Gelius and Lecomte, 2000). The key point is that these PSFs can be calculated with relatively low computational effort with the use of ray tracing. This feature has been used to simulate efficiently 2D and 3D PSDM images with the method called *simulated prestack local imaging* (SimPLI) described, for example in Lecomte and Guerin (2005) and Lecomte (2008). The concept of PSF can also be used to enhance the resolution of PSDM images through 2D deconvolution methods. This approach has been explored in works such as Gelius et al. (2002) and Sjoeberg et al. (2003). However, these works only consider the use of a smaller subsection along the vertical direction of each PSF.

In this paper, we start by reviewing the key topics on the use of 2D deconvolution to enhance the resolution of seismic PSDM images (Gelius and Lecomte, 2000; Gelius et al., 2002; Lecomte, 2008). Next, we introduce a 2D filtering approach based on spiking deconvolution. This contrasts with previous works, such as Sjoeberg et al. (2003), in which an inversion approach was used. Finally, we present numerical results performed on controlled data, and discuss the potentials and the limitations of the method.
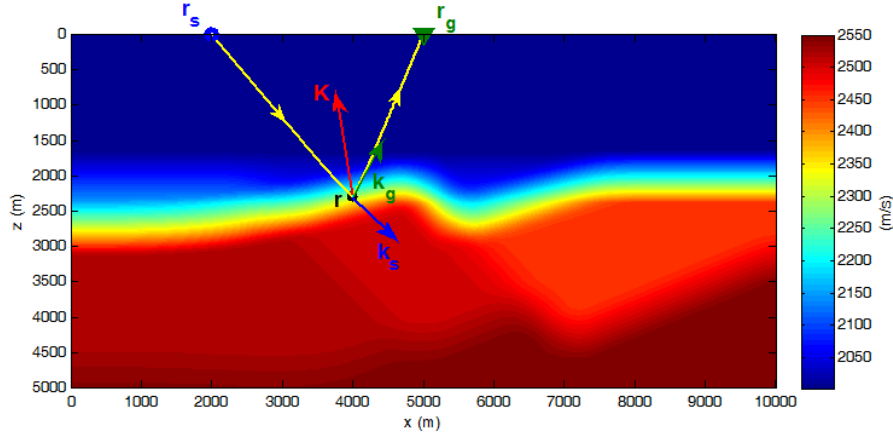
Figure 1: *A smooth velocity field corresponding to a simple fault system and a point scatterer located at* **r**. *The source and receiver are located, respectively, at* $\mathbf{r}_s$ *and* $\mathbf{r}_g$. *The local directions of the Green's functions of the incident and scattered wavefields are given by* $\mathbf{k}_s$ *and* $\mathbf{k}_g$ *and* $\mathbf{K}$ *is the corresponding scattering wavenumber.*

THE RESOLUTION FUNCTION AND THE POINT SPREAD FUNCTION

Let $\gamma(\mathbf{r})$ be a quantity which characterizes a geological model, such as the reflectivity, at a given point $\mathbf{r}$. As described in Gelius et al. (2002), its resolution is controlled by the Fourier vector associated with the model space that is called *scattering wavenumber*, which is again closely linked to the derivation of the resolution function. In the referred work, both a smooth acoustic or scalar velocity model (as shown in Figure 1) and local reaction are assumed. This means that the scattering or reflection at a given model point $\mathbf{r}$ is only caused by interactions within a surrounding small region Ω, being negligible the interactions with other parts of the model. A local plane-wave contribution is also assumed, as pointed out in Gelius and Lecomte (2000). Given these assumptions, the spatial Fourier transform of $\gamma(\mathbf{r})$ is defined as

$$\Gamma(\mathbf{K}) = \int_{\Omega} \gamma(\mathbf{r}') \exp(-j\mathbf{K} \cdot \mathbf{r}') d\mathbf{r}'. \tag{1}$$

Here, $\mathbf{K}$ denotes the Fourier vector, or the scattering wavenumber vector, as mentioned before, at the center point $\mathbf{r}$. As shown in Figure 1, and following Gelius et al. (2002), this vector can be linked to the seismic survey geometry by the relationship

$$\mathbf{K} = -\omega \nabla \tau(\mathbf{r}_g, \mathbf{r}_s, \mathbf{r}) = -\omega[\nabla \tau_s(\mathbf{r}) + \nabla \tau_g(\mathbf{r})] = -\mathbf{k}_s(\mathbf{r}) + \mathbf{k}_g(\mathbf{r}). \tag{2}$$

In the above equation, $\mathbf{r}_g$ and $\mathbf{r}_s$ denote, respectively, the positions of the receiver and source, ω is the angular frequency, τ is the total traveltime and τ_s and τ_g are, respectively, the traveltimes along the rays from the source at $\mathbf{r}_s$ to the model point at $\mathbf{r}$ and from the model point to the receiver at $\mathbf{r}_g$. In addition, the wavenumber vectors $\mathbf{k}_s$ and $\mathbf{k}_g$ represent the local directions of the source and receiver Green's functions respectively. These Green's functions must be calculated in the background model. In case of complete coverage in the Fourier space, it follows from Equation (1) that $\gamma(\mathbf{r})$ can be obtained by the inverse Fourier transform of $\Gamma(\mathbf{K})$, i.e.,

$$\gamma(\mathbf{r}) = \int \Gamma(\mathbf{K}) \exp(j\mathbf{K} \cdot \mathbf{r}) d\mathbf{K}. \tag{3}$$

Unfortunately, as can be inferred from Figure 1, the range of directions of $\mathbf{K}$ is constrained by the limited number of source and receiver positions at the surface, i.e., a 360° coverage is, in practice, not possible. Moreover, from Equation (2) we see that the bandwidth limitations imposed by the source signature in combination with attenuation effects, impose a constraint on the length of $\mathbf{K}$, which is proportional to ω. If we describe these actual band limitations by $\Theta(\mathbf{K})$, the actual estimated model parameter $< \gamma(\mathbf{r}) >$ can

be expressed as

$$< \gamma(\mathbf{r}) > = \int \Theta(\mathbf{K})\Gamma(\mathbf{K})\exp(j\mathbf{K}\cdot\mathbf{r})d\mathbf{K}. \tag{4}$$

Substituting (1) in (4), we have:

$$< \gamma(\mathbf{r}) > = \int_{\Omega} \gamma(\mathbf{r}') \left[\int \Theta(\mathbf{K})\exp(j\mathbf{K}(\mathbf{r}-\mathbf{r}'))d\mathbf{K} \right] d\mathbf{r}' = \int_{\Omega} \gamma(\mathbf{r}')RF(\mathbf{r}-\mathbf{r}')d\mathbf{r}', \tag{5}$$

where $RF(\mathbf{r})$ is defined by the inner integral (between brackets) in the above equation. In fact, $RF(\mathbf{r})$ is the resolution function, which describes the distortions of the estimated model. Moreover, inspection of Equation (5) shows that the relationship between $\gamma(\mathbf{r})$ and $< \gamma(\mathbf{r}) >$ is described by a 2D convolution between the actual model quantity, $\gamma(\mathbf{r})$, and $RF(\mathbf{r})$. As $RF(\mathbf{r})$ can be seen as the impulse response of a linear system at the point $\mathbf{r}$, i.e., a measure of how a point scatterer blurs or spreads, it is also called *Point Spread Function* (PSF). This applies for Born scattering, in which it is assumed that every discontinuity of the model can be approximated by a point scatterer.

THE RELATIONSHIP BETWEEN PSDM AND PSF

The aim of depth migration is to locate in depth the information recorded in time. In order to do so, it relies on the velocity field and the traveltimes, representing the link between the time and depth domains. For illustration purposes, a homogeneous model is considered. Figures 2(a) and 2(b) show the one way traveltimes from a source located at $\mathbf{r}_s$ and a receiver at $\mathbf{r}_g$. Such traveltimes are denoted, respectively, by $\tau_s(\mathbf{r},\mathbf{r}_s)$ and $\tau_g(\mathbf{r}_g,\mathbf{r})$. Note that the curves with constant traveltime values represent the wavefronts. Figure 2(c) shows the scattering traveltimes, $\tau(\mathbf{r}_g,\mathbf{r}_s,\mathbf{r}) = \tau_s(\mathbf{r},\mathbf{r}_s) + \tau_g(\mathbf{r}_g,\mathbf{r})$, which link depth and time when considering the backscattered energy emitted at $\mathbf{r}_s$ and received at $\mathbf{r}_g$. The points of the image where $\tau(\mathbf{r}_g,\mathbf{r}_s,\mathbf{r})$ is constant form the *scattering isochrones*. In a homogeneous medium, they have an elliptical shape, with foci located at $\mathbf{r}_s$ and $\mathbf{r}_g$. If a single trace and a single scatterer are considered, as shown in

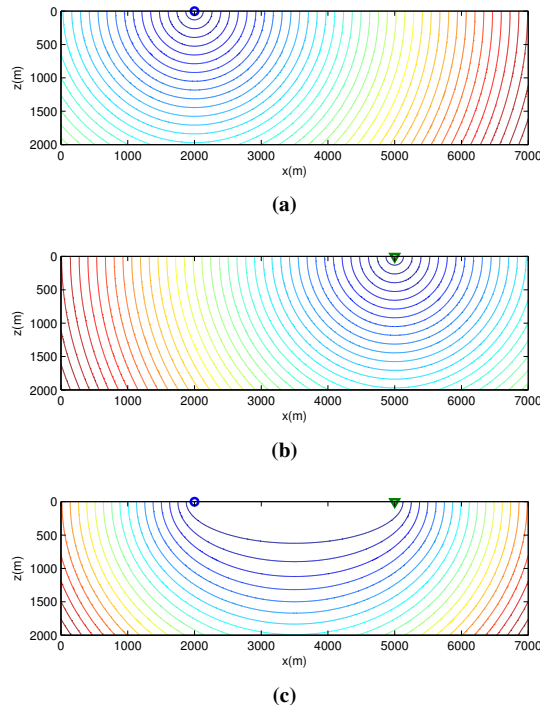**(a)**

(b)

(c)

Figure 2: *Isotraveltimes from source (a), receiver (b) and isochrones (c).*

Figures 3(a) and 3(b), the migrated image will be the isochrone which contains the scatterer (indicated
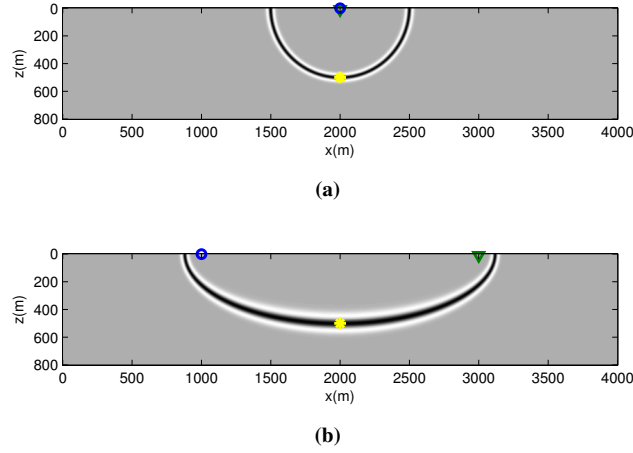
(a)

(b)

Figure 3: *Impulse response of the PSDM algorithm in a homogeneous medium. The yellow star corresponds scatterer position. Blue circles and green triangles correspond, respectively, to the sources and receivers: (a) PSDM for a single ZO trace; (b) PSDM for a single trace with offset 2000m.*

with a yellow star). In Figure 3(a) the source and receiver coincide (zero offset, ZO) and are just above the point scatterer. The resulting image is a circle (an ellipse with coinciding foci) with constant width. In Figure 3(b) an offset exists between the source and receiver, so the migrated image has an elliptical shape, wider than in the ZO case and also with a varying width. These type of images are examples of impulse responses of the PSDM algorithm.

Figure 4(a) is the result of the sum of different impulse responses calculated for different ZO traces with a single scatterer. Observe that there is a constructive interference at the point-scatterer location, while destructive interference at other points. Figure 4(b) is the corresponding result for a common-shot gather. By comparing these two images, we observe that the resulting patterns are different, in spite of the fact that the same scatterer and pulse were used. Thus, the use of two different acquisition geometries produced two different PSFs. Note that, ideally, the migrated image should show only the point scatterer. However, as mentioned before, distortion is caused by the use of a finite number of traces, which implies limited aperture, and also by limited frequency bandwidth. From the foregoing discussion, we see that it may be possible to estimate a PSF by migrating the measured data associated with a point scatterer. However, this is very costly, since it involves the use of prestack synthetic data followed by migration. According to Lecomte (2008), howeve, such procedure is the only alternative when it comes to wave-type migration. For migration methods of Kirchhoff type, in which a local interaction assumption is considered, a scattering wavenumber vector approach, as introduced in Equation (2), can be applied with much less cost upon the use of ray tracing.

To demonstrate this claim, we start by considering the *illumination vector*, $\mathbf{I}(\mathbf{r}_g, \mathbf{r}_s, \mathbf{r})$. It is defined as

$$\mathbf{I}(\mathbf{r}_g, \mathbf{r}_s, \mathbf{r}) = \mathbf{p}_g(\mathbf{r}_g, \mathbf{r}) - \mathbf{p}_s(\mathbf{r}, \mathbf{r}_s) = \frac{1}{c(\mathbf{r})}\left[\hat{\mathbf{u}}_g(\mathbf{r}_g, \mathbf{r}) - \hat{\mathbf{u}}_s(\mathbf{r}, \mathbf{r}_s)\right], \qquad (6)$$

where $\hat{\mathbf{u}}_s$ and $\hat{\mathbf{u}}_g$, are unit vectors, evaluated at the image point, $\mathbf{r}$, that are perpendicular, respectively, to the wavefront incident from the source at $\mathbf{r}_s$ and to the one scattered and received at $\mathbf{r}_g$. In Equation (6), $c(\mathbf{r})$ is the velocity at the image point $\mathbf{r}$ and $\mathbf{p}_s(\mathbf{r}, \mathbf{r}_s)$ and $\mathbf{p}_g(\mathbf{r}_g, \mathbf{r})$ are the slowness vectors associated with the wavefields. From the eikonal equation, we also have:

$$\nabla\tau_s(\mathbf{r}, \mathbf{r}_s) = \mathbf{p}_s(\mathbf{r}, \mathbf{r}_s) \text{ and } \nabla\tau_g(\mathbf{r}_g, \mathbf{r}) = -\mathbf{p}_g(\mathbf{r}_g, \mathbf{r}). \qquad (7)$$

Therefore, by substituting (7) in (6) and comparing the result with (2), the relationship between the illumination vector and the scattering wavenumber vector is found to be

$$\mathbf{K} = \omega\mathbf{I}(\mathbf{r}_g, \mathbf{r}_s, \mathbf{r}). \qquad (8)$$
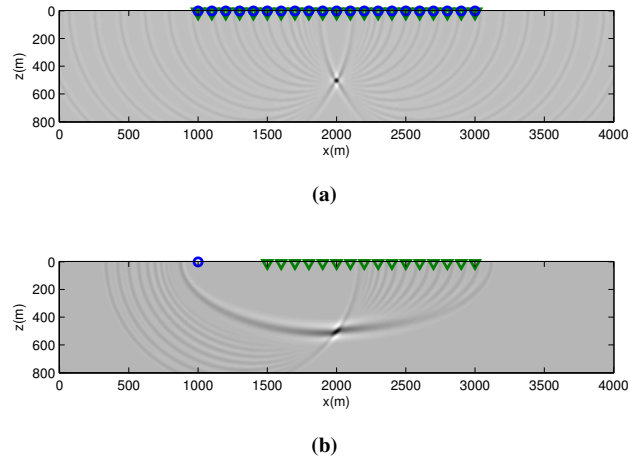
(a)

(b)

Figure 4: *Migrated image of complete trace gathers. The blue circles and the green triangles correspond, respectively, to the sources and receivers. The velocity model is homogeneous: (a) PSDM for ZO gather; (b) PSDM for common-shot gather.*

Also, it follows that

$$\mathbf{I}(\mathbf{r}_g, \mathbf{r}_s, \mathbf{r}) = -\nabla \tau(\mathbf{r}_g, \mathbf{r}_s, \mathbf{r}). \tag{9}$$

Figure 6 sketches how the slowness vectors can be easily computed with the use of ray tracing techniques, since they are tangent to the ray paths which meet at the image point. As shown in Lecomte and Gelius (1998), $\mathbf{K}$ is perpendicular to the local plane wavefront tangent to the scattering isochrone and is its representation in the wavenumber domain. If a single temporal frequency ω_0 is considered, Equation (8) represents the 2D Fourier Transform (2DFT) of a monochromatic plane wave (a point in the wavenumber domain). If a pulse with limited bandwidth, as shown in Figure 5(a), is considered, all frequencies are mapped to the wavenumber domain along the scattering wavenumber vectors according to Equation (8) and shown in Figure 5(b). Figure 5(c) shows the Fourier amplitudes of the wavelet along the scattering wavenumber vector indicated in red in Figure 5(b). The amplitudes are symmetric with respect to the origin, since both positive and negative frequencies are considered here. This spectrum represents a band-limited plane wave in the space domain as the one displayed in Figure 5(d).

2D PSF ESTIMATION

As Equation (8) and also the discussion in the previous section suggest, the PSF at a point of a PSDM image may be calculated, whenever a velocity field and a pulse amplitude spectrum are given. Namely, in algorithmic form we have:

Step 1: Select an image point.

Step 2: For each trace (source-receiver pair) do:

Step 2.1: Estimate the scattering isochrones and the illumination vector.

Step 2.2: Map the amplitude spectrum in the wavenumber domain according to Equation (8) and Figures 5(a)-5(c) to obtain the corresponding scattering wavenumber vector.

Step 3: Since the PSDM image represents the superposition of impulse responses (such as the ones shown in Figures 4(a) and 4(b)), the scattering wavenumber vectors corresponding to each trace are to be summed. This result gives the PSF in the wavenumber domain.

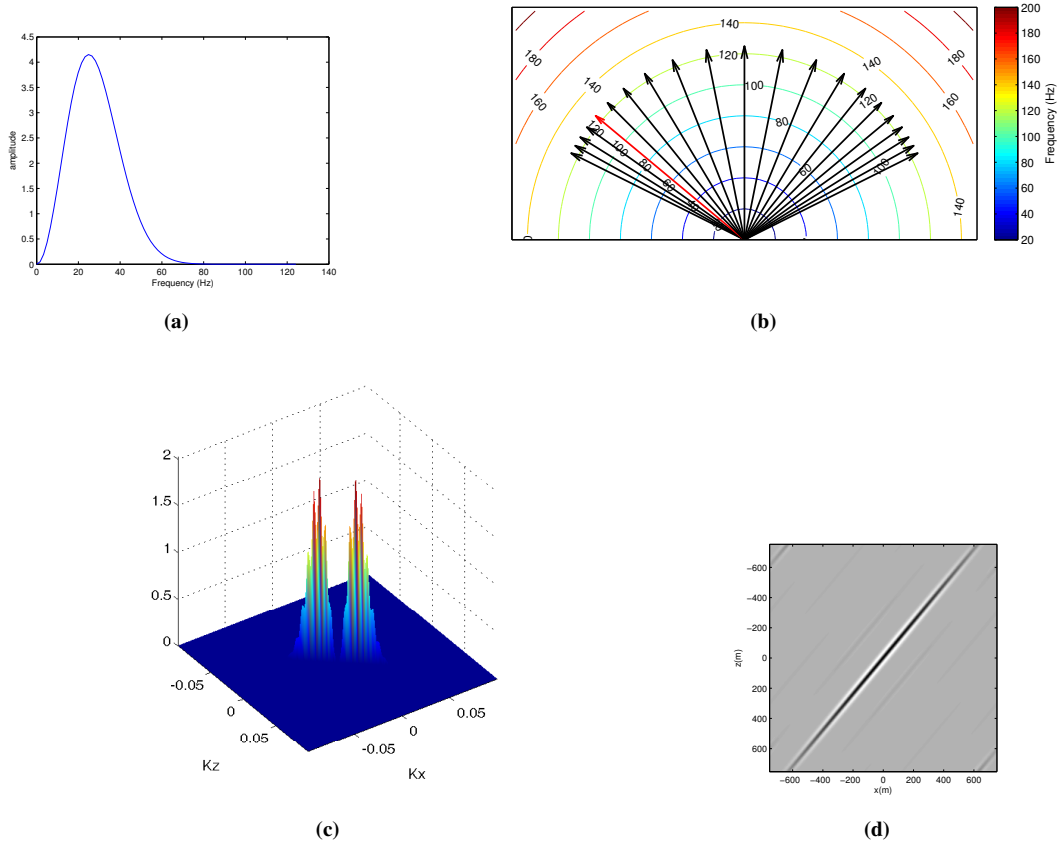Step 4: Transform the PSF from the wavenumber domain to the space domain.

(a)   **(b)**

(c)   **(d)**

Figure 5: *Frequency mapping into the wavenumber domain: (a) The amplitude spectrum of a Ricker wavelet with central frequency of 25Hz; (b) Scattering wavenumber vectors for the survey in Figure 5(a). The sampling rate is 4ms, so that the maximum frequency is 125Hz; (c) Fourier amplitudes of the Ricker wavelet of Figure 5(a) mapped onto the scattering wavenumber vector displayed in red in Figure 5(b) and (d) Band limited plane wave corresponding to the spectrum in (c).*

In our implementation, the isochrone estimation in Step 2.1 was done with the aid of an eikonal solver, developed by Podvin and Lecomte (1991). An implementation in C is available on the internet as the package FDTIMES (Podvin, 2006). Given a velocity field and a source location, the solver finds the solution for the eikonal equation in isotropic acoustic media. Thus, it provides the traveltime of the first arriving wavefront for all points of the model, as shown in Figure 6. In this figure, a secondary source located in the subsurface of the velocity model presented in Figure 1 was simulated. The rays to the source and receiver at the surface were traced using the traveltime gradients. Such rays are perpendicular to the wavefronts. The eikonal solver was also used in the homogeneous model ($C = 1500m/s$) analyzed in Figure 2(c). The scattering traveltimes, $\tau(\mathbf{r}_s, \mathbf{r}_g, \mathbf{r})$, were obtained as the sum of the source and receiver traveltimes to the image point (see Figures 2(a) and 2(b)). As an illustration, Figures 7(a) and 7(b) show several PSFs calculated for points along the isochrones (impulse responses) in Figures 3(a) and 3(b). The illumination vectors, $\mathbf{I}$, and slowness vectors, $-\mathbf{p}_s$ and $\mathbf{p}_g$, are also plotted. By comparing these figures, it is possible to confirm that the PSFs are good local plane approximations of the isochrones, as expected. This can readily be interpreted if we recast Equation (6) in the form

$$\mathbf{I}(\mathbf{r}_g, \mathbf{r}_s, \mathbf{r}) = \frac{2\cos(\theta/2)}{c(\mathbf{r})} \hat{\mathbf{u}}(\mathbf{r}_g, \mathbf{r}_s, \mathbf{r}), \tag{10}$$

where θ is the opening angle between $-\mathbf{p}_s$ and $\mathbf{p}_g$. It is interesting to notice that $\mathbf{I}(\mathbf{r}_g, \mathbf{r}_s, \mathbf{r})$ has a maximum length of $2/c(\mathbf{r})$ when $\theta = 0$, namely in case of normal-incidence backscattering. This can be observed in
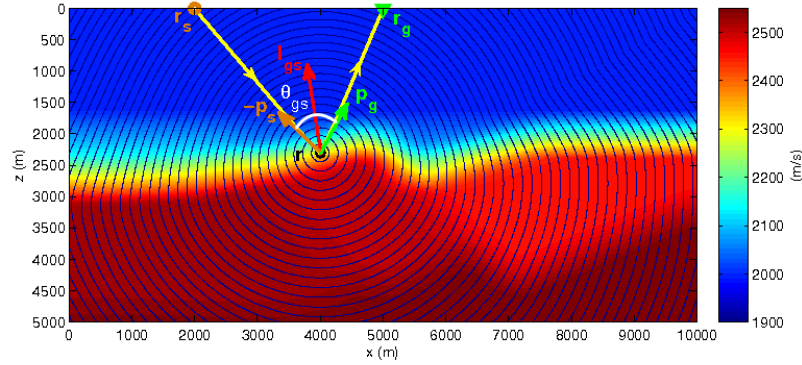
Figure 6: *Same setting as in Figure 1:* $\mathbf{I}$ *is the illumination vector and* θ *is the opening angle between* $-\mathbf{p}_s$ *and* $\mathbf{p}_g$*. The first arriving wavefronts from a secondary source at the point scatterer are displayed.*

Figure 7(a), where the PSFs were calculated along an isochrone corresponding to the zero offset scenario presented in Figure 3(a). In this case, $\theta = 0$ at all points of the isochrone and the size of the illumination vector, plotted in red in Figure 7(a), is constant. As a consequence, the thickness of the migrated trace in Figure 3(a) is also constant along the isochrone. As indicated by Equation (10), the size of $\mathbf{I}(\mathbf{r}_g, \mathbf{r}_s, \mathbf{r})$ decreases as θ increases. This can be observed in Figure 3(a), where the PSFs were calculated along the isochrone corresponding to the common shot scenario presented in Figure 3(b). In this case, the angle is wider at the bottom of the isochrone. Thus, the illumination vector is smaller in this region and, as shown in Figures 3(a) and 3(b), the resolution is better in the regions closer to the receiver or the source and it becomes worse near the bottom.

As a next illustration, we compute the illumination vectors for the acquisition geometries in Figures 4(a) and 4(b). These are displayed, at the point-scatterer position, in Figures 15(b) and 18(a). For the ZO case of Figure 15(b), we have $\theta = 0$ and the illumination vector has the maximum length for all directions. For the common-shot situation of Figure 18(a), the size of the illumination vector decreases as the offset and θ increases, indicating a poorer resolution at the larger offsets. This becomes evident by looking at the corresponding PSFs shown in Figures 15(a) and 9(b). We clearly see an improved resolution for the ZO case (Figure 9(a)) when compared to the common-shot counterpart (9(b)). The same comparison can be made when we consider the blur patterns observed in the actual PSDM images in Figures 4(a) and 4(b).

2D DECONVOLUTION

In this section, we derive a method to improve the resolution of an image by mitigating the effects of the PSF. This method will be implemented in the discrete domain, so we begin by defining discrete, i.e., sampled versions of the variables involved in the problem and their relationship. For that matter, let $y(m, n) = < \gamma(m\Delta x, n\Delta z) >$ be the sampled PSDM image, where Δx and Δz are the spatial sampling intervals along x and z, respectively. Also, let $x(m, n) = \gamma(m\Delta x, n\Delta z)$ be the discrete version of the quantity of interest. Using the 2D convolution model in equation (5), we can approximate the relationship between $y(m, n)$ and $x(m, n)$ as a 2D discrete convolution:

$$y(m, n) = \sum_{k=-K}^{K} \sum_{l=-L}^{L} h(k, l)x(m - k, n - l), \tag{11}$$

where $h(m, n) = RF(m\Delta x, n\Delta z)$ is the discrete version of the PSF.

Note that, in Equation (11), it is assumed that the PSF is such that the estimated parameter $y(m, n)$ depends on the actual parameter $x(m, n)$ only in a $(2K + 1) \times (2L + 1)$ region centered at the point (m, n). Furthermore, it is assumed that the velocity field is smooth and that the area of interest is small enough that the PSF is the same for all points in the area.
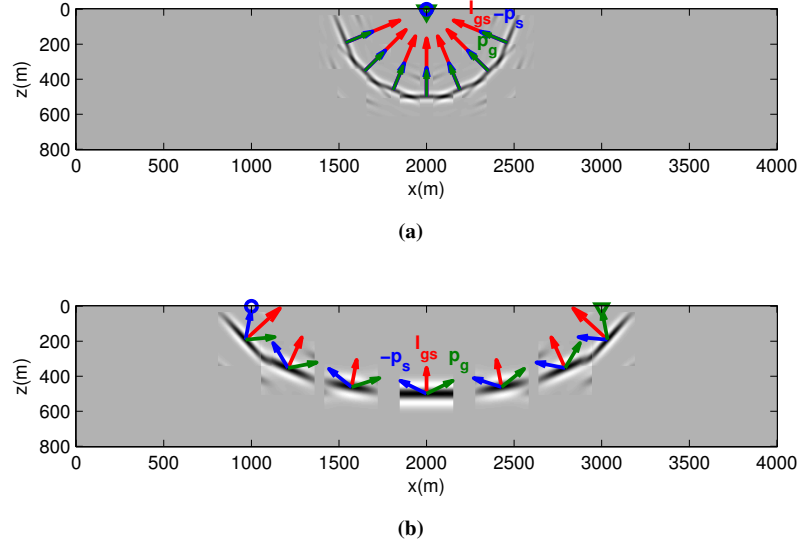
(a)

(b)

Figure 7: *PSFs calculated along two migrated traces corresponding to the acquisition geometries in Figures 3(a) and 3(b). The blue, red and green vectors correspond respectively to $-\mathbf{p}_s, \mathbf{I}$ and $\mathbf{p}_g$: (a) Migrated ZO trace; (b) Migrated trace with offset 2000m.*

Our goal now is to produce a good estimate of $x(m, n)$ at a point (m, n), based on values of y in a neighborhood of this point. To begin with, we adopt the so-called lexicographic vector representation of a matrix, and introduce the vectors $\mathbf{x}(m, n)$ and $\mathbf{y}(m, n)$ (cf. Figure 10). The vector $\mathbf{y}(m, n)$ contains all the pixels of a $(2P + 1) \times (2Q + 1)$ sub-image of the PSDM result centered at (m, n) that are used to estimate $x(m, n)$. In the same way, the vector $\mathbf{x}(m, n)$ contains the values of the actual parameter in a $(2(P + K) + 1) \times (2(Q + L) + 1)$ neighborhood around (m, n). Equation (11) can be, thus, recast as

$$\mathbf{y}(m, n) = \mathbf{H}\mathbf{x}(m, n). \tag{12}$$

To deconvolve the blurring effect, we introduce a filtering matrix $\mathbf{W}$ in Equation (12) as follows:

$$\mathbf{W}\mathbf{y}(m, n) = \mathbf{W}\mathbf{H}\mathbf{x}(m, n) = \tilde{\mathbf{x}}(m, n). \tag{13}$$

In order for the estimate $\tilde{\mathbf{x}}$ to be as close as possible to $\mathbf{x}$, we need

$$\mathbf{W}\mathbf{H} \approx \mathbf{I}. \tag{14}$$

Equation (14) represents the 2D analogy of the well-known *spiking deconvolution problem* (see, e.g., Yilmaz, 2001). Thus, it is rather straightforward to find a least-squares filter matrix $\mathbf{W}$ that corresponds to the matrix $\mathbf{H}$. As in the 1D spiking deconvolution case, a regularization term is introduced to avoid amplification of spectral notches.

NUMERICAL RESULTS

Homogeneous medium

Initially, a mono trace configuration with offset equal to 2000m and a single scatterer is considered. The velocity of the medium is $C = 2000$m/s and a Ricker wavelet with center frequency of 25Hz is used. Figure 11(a) shows the diffraction-stack migration of this trace (Yilmaz, 2001). Three possible scatterer positions are displayed as red crosses. Figures 11(b)-11(d) show the results of 2D deconvolution for the PSFs estimated at each cross. The corresponding PSFs are shown in Figures 12(a)-12(c). It is observed that
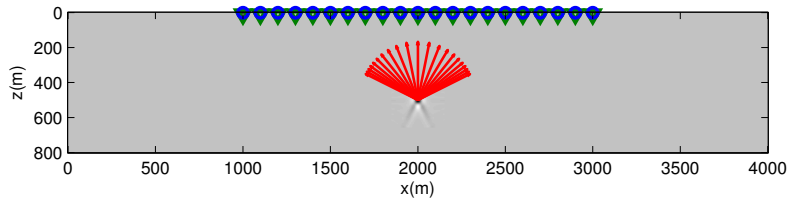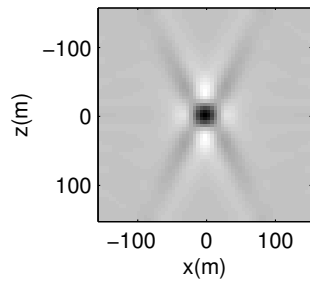
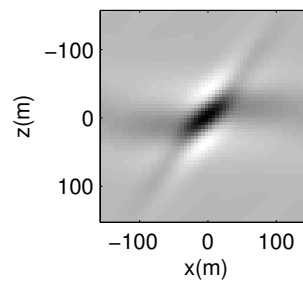**(a)** *Illumination vectors calculated at the scatterer for a ZO geometry*
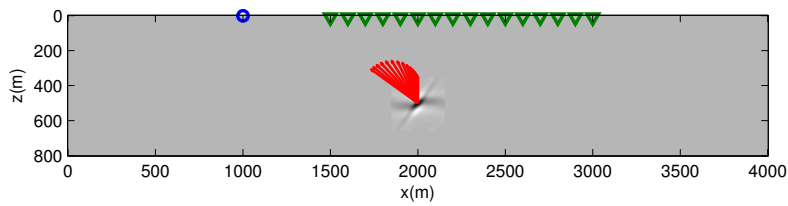
(b) *Illumination vectors calculated at the scatterer for a common-shot geometry*

Figure 8: *Illumination vectors for acquisition geometries of Figures 4(a) and 4(b).*

(a) *PSF corresponding to Figure 8(a).*

(b) *PSF corresponding to Figure 8(b).*

Figure 9: *PSFs calculated at the scatterer for the acquisition geometries: (a) ZO of Figure 4(a) and (b) Common shot of 4(b).*

$$\begin{bmatrix} y(m-1,n-1) & y(m-1,n) & y(m-1,n+1) \\ y(m,n-1) & y(m,n) & y(m,n+1) \\ y(m+1,n-1) & y(m+1,n) & y(m+1,n+1) \end{bmatrix} \rightarrow \begin{bmatrix} y(m-1,n-1) \\ y(m-1,n) \\ y(m-1,n+1) \\ y(m,n-1) \\ y(m,n) \\ y(m,n+1) \\ y(m+1,n-1) \\ y(m+1,n) \\ y(m+1,n+1) \end{bmatrix} = \mathbf{y}(m,n)$$

Figure 10: *Lexicographic representation of an image matrix.*

the resolution is increased near the scatterers, however the remaining part of the isochrone gets distorted. This is due to the fact that the PSF changes along the isochrone, as shown in Figures 7(a) and 7(b). The assumption of a spatially invariant PSF is, thus, not globally correct.

On the other hand, if a small target region is considered and the velocity field is smooth enough, it
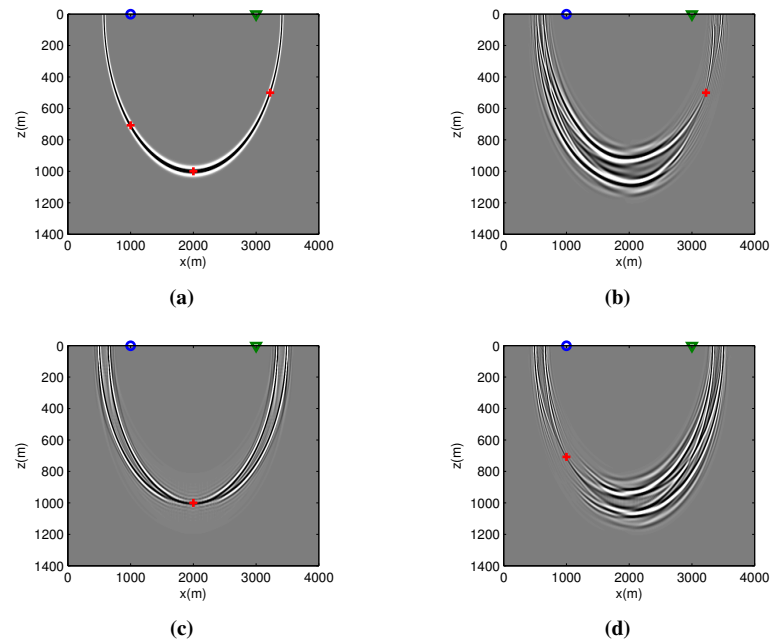
(a)

(b)

(c)

(d)

Figure 11: *(a) Migrated single trace with offset 2000m. Red crosses represent three possible locations for scatterers; (b)-(d) Results of 2D deconvolution with PSFs estimated at each red cross.*
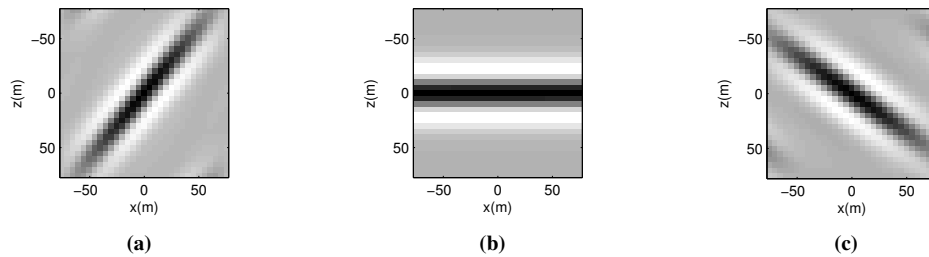

(a)

(b)

(c)

Figure 12: *PSFs used to obtain the 2D deconvolution results shown in, respectively: (a) Figure 11(b); (b) Figure 11(c) and (c) Figure 11(d).*
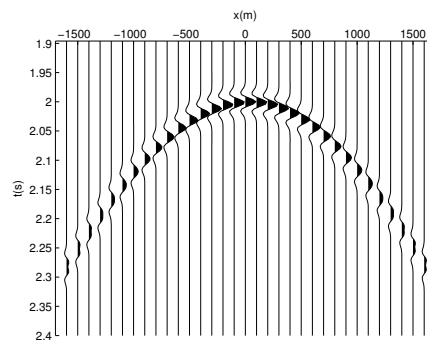

Figure 13: *Common-shot gather of two nearby scatterers located at $(-20, 2000)^T$ and $(30, 2000)^T$. The velocity is $C = 2000$m/s.*

becomes reasonable to assume that the PSF is invariant in space. As an example, consider a scenario with two nearby scatterers. They are located at $(-20, 2000)^T$ and $(30, 2000)^T$ (coordinate system $(x, z)^T$). A common-shot gather with source at the origin and the receivers ranging from $(-1600, 0)^T$ to $(1600, 0)^T$ (10m spacing), is migrated by diffraction stacking (cf. Figure 13). The result is shown Figure 14(a), in which we see that it is not possible to discriminate the two scatterers. However, the use of 2D deconvolution technique, as shown in Figure 14(c), allows to discriminate the two scatterers. Thus, the use of 2D deconvolution enables increased lateral resolution. The 1D deconvolution was also tested by considering just the central vertical part of the PSF, as in (Gelius et al., 2002). The result is displayed in Figure 14(b). In this case, the lateral resolution is slightly increased, but the 2D deconvolution provides a better separation between the scatterers, as expected.

The above 2D deconvolution result is comparable to the one presented in Gelius et al. (2013), shown in Figure 14(d), in which a high resolution method called multiple signal classification (MUSIC) was used for the same data. The main difference is that MUSIC is rather a localization technique and its use implies the loss of amplitude information. That does not happen with the deconvolution technique. On the other hand, the result provided by MUSIC is more accurate in the sense that it does not show the migration artifacts and the ringing observed in the deconvolved image.
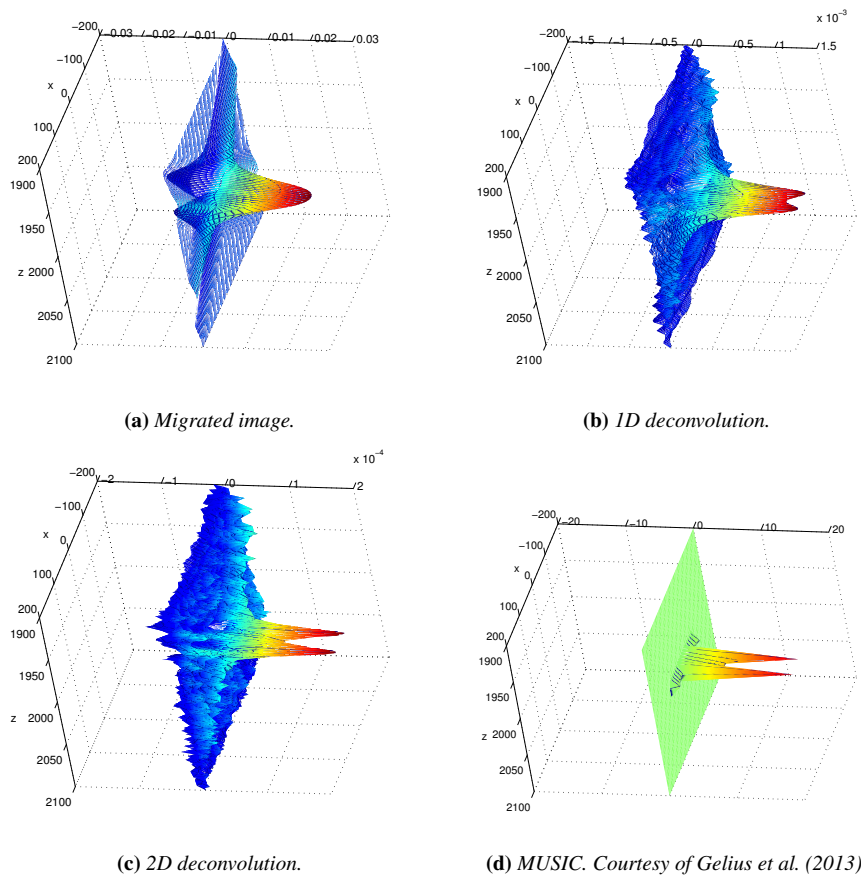
(a) *Migrated image.*

(b) *1D deconvolution.*

(c) *2D deconvolution.*

(d) *MUSIC. Courtesy of Gelius et al. (2013).*

Figure 14: *Migrated, deconvolved and MUSIC images of two nearby scatterers.*

Fault system

A fault model with layers of different velocities is now considered, as shown in Figure 15(a). This model represents the original velocities before smoothing as shown in Figures 1 and 6. A common offset section (4000m), whose acquisition geometry is described in Figure 15(a), was obtained using 2D ray tracing (NORSAR software package). In the figure, a smaller target area has been selected for later migration.
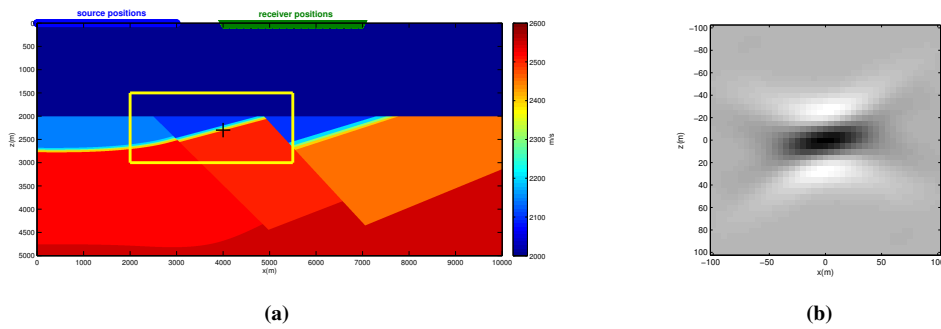
(a)

(b)

Figure 15: *(a) Fault system model: The selected target is highlighted with a yellow box. The black cross describes the point where the PSF for the 2D deconvolution is calculated. (b) The PSF calculated at the position indicated by the black cross.*
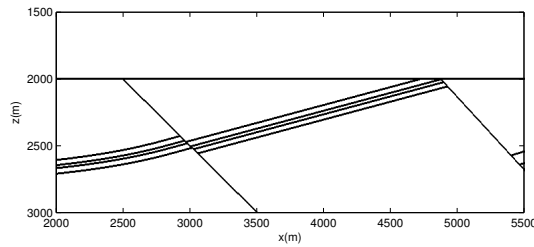

Figure 16: *The interfaces in the selected target.*

The PSF, shown in Figure 15(b) is calculated at the position indicated by a black cross in Figure 15(a). The diffraction-stack migration of the small rectangle in Figure 15(a) is shown in Figure 17(a). Observe that from the four inclined reflectors displayed in Figure 16, only three of them are now visible. The 2D deconvolution method was then applied to the migrated image. The result is shown in Figure 17(b). As
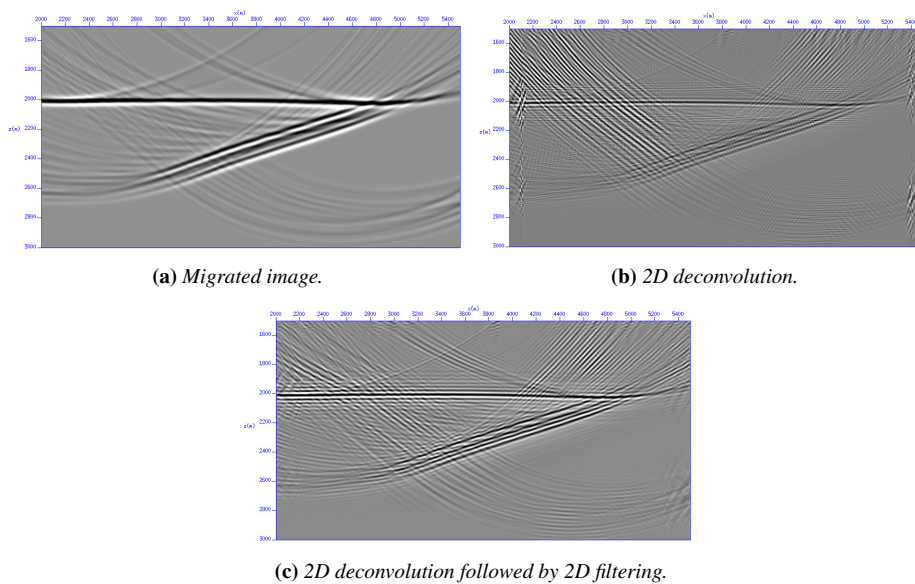

(a) *Migrated image.*

(b) *2D deconvolution.*

(c) *2D deconvolution followed by 2D filtering.*

Figure 17: *Migrated and deconvolved images.*

can be seen in this figure, all four reflectors were now resolved. However, it is also observed that the orig-

inal migration artifacts in Figure 17(a) have been somewhat amplified. Also, some ringing is associated with the reflectors. This can be partly explained by observing the 2DFT amplitude spectrum of the PSF in Figure 18(a). As the 2D spiking deconvolution filter optimizes the inversion of the PSF in the mean squares sense, it enhances the low amplitude frequencies of the PSF. Since the PSF has null wavenumber components at the points which are not covered by the scattering wavenumber vectors (determined by the acquisition geometry, velocity model and the seismic frequency band), a high gain is associated with these directions. As these frequency components are associated with non-existing illumination directions and temporal frequencies of the actual data, their enhancement leads to the undesired effects as seen in Figure 17(b). This is supported by the comparison between the 2DFT amplitude spectra of the migrated image
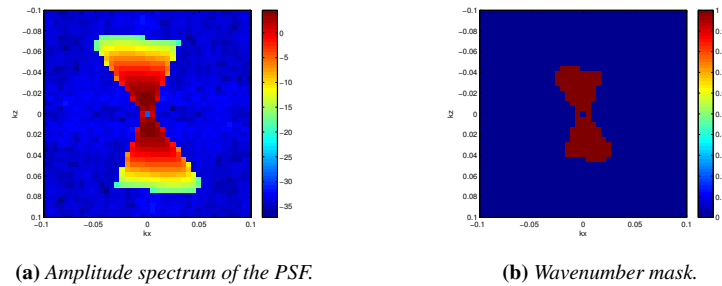

(a) *Amplitude spectrum of the PSF.*   **(b)** *Wavenumber mask.*

Figure 18: *(a) 2DFT amplitude spectrum of the PSF used for 2D deconvolution and (b) the wavenumber mask used to filter the deconvolved image.*

and the deconvolved image, shown respectively in Figures 19(a) and 19(b). For the migrated image, most of the energy is located around the origin and within the limits of the "band" associated with the 2DFT amplitude spectrum of the PSF seen in Figure 18(a). On the other hand, the 2DFT amplitude spectrum of the deconvolved image shows high amplitudes along a band around the k_x and k_y axes which continue to the edges of the spectra, and indicates the presence of high frequency artifacts, as seen in Figure 17(b). In order to eliminate these components, a 2D filter calculated from a wavenumber mask displayed in Figure 18(b) was used. The 2DFT amplitude spectrum in Figure 18(b) was transformed to the space domain and the resulting filter was applied to the deconvolved image. The result is displayed in Figure 17(c). It is possi-
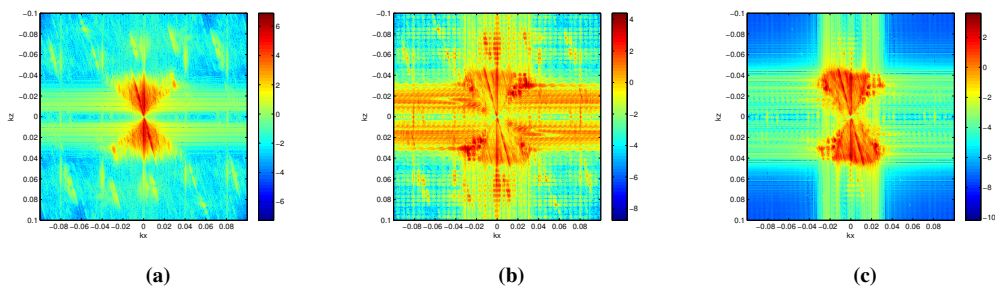

(a)   **(b)**   **(c)**

Figure 19: *2DFT amplitude spectrum of the migrated and deconvolved images: (a) Migrated image; (b) After the 2D deconvolution and (c) After the 2D deconvolution followed by 2D filtering.*

ble to observe in the resulting image that the artifacts and the high frequency ringing that were dimming the reflectors have now been attenuated. Also, in the resulting amplitude spectrum, in Figure 19(c), the high wavenumber components, i.e., the components outside the wavenumber band of the PSF have been attenuated.

DISCUSSION AND CONCLUSIONS

This paper starts with a review of the resolution or point spread function and continues by establishing a convolutional model to describe the blurring of a seismic PSDM image. During this discussion, the

link between PSDM and PSFs, as well as an actual PSF estimation, were described. Next, a 2D spiking deconvolution technique was introduced to remove the blurring effect. It was applied to various types of migrated synthetic data. It was shown for a homogeneous medium case that the use of 2D deconvolution improves the lateral resolution of migrated images. In fact, the results were comparable to the one obtained by methods of high resolution such as MUSIC when it comes to separation of two nearby point scatterers (diffraction limited case). The results for a layered fault model demonstrated that the method is also able to enhance the resolution of reflectors. However, already existing migration artifacts can possibly be further enhanced by the deconvolution if it is not done with care. A refinement was already proposed with the implementation of a 2D filter based on a 2D wavenumber mask. Further improvements could also include, e.g., the post-processing of the PSFs considering the Fresnel zone of the reflectors and appropriate tapering in order to attenuate the residual ringing. In case of reflections, the use of a locally determined *reflector spread function* (Kirchhoff type) instead of the Born or point spread type of resolution function will also further improve the result (Gelius et al., 2002).

REFERENCES

Banham, M. and Katsaggelos, A. (1997). Digital image restoration. *Signal Processing Magazine, IEEE*, 14(2):24 –41.

Gelius, L.-J. and Lecomte, I. (2000). The resolution function in linearized Born and Kirchhoff inversion. In Hansen, P., Jacobsen, B., and Mosegaard, K., editors, *Methods and Applications of Inversion*, volume 92 of *Lecture Notes in Earth Sciences*, pages 129–141. Springer Berlin Heidelberg.

Gelius, L.-J., Lecomte, I., and Tabti, H. (2002). Analysis of the resolution function in seismic prestack depth imaging. *Geophysical Prospecting*, 50(5):505–515.

Gelius, L.-J., Tygel, M., Takahata, A. K., Asgedom, E. G., and Serrano, D. R. (2013). *High-resolution imaging of diffractions - a steered MUSIC approach*. WIT annual report.

Lecomte, I. (2008). Resolution and illumination analyses in psdm: A ray-based approach. *The Leading Edge*, 27(5):650–663.

Lecomte, I. and Gelius, L.-J. (1998). Have a look at the resolution of prestack depth migration for any model, survey and wavefields. *SEG Extended Abstracts*, pages 1112–1115.

Lecomte, I. and Guerin, L. P. (2005). Simulated 2d/3d psdm images with a fast, robust, and flexible fft-based filtering approach. *SEG Extended Abstracts*, pages 1810–1813.

Podvin, P. (2006). *FDTIMES : Computation of seismic travel times by finite-differences*. http://www.geophy.mines-paristech.fr/soft/fdtimes/html_doc/index.html.

Podvin, P. and Lecomte, I. (1991). Finite difference computation of traveltimes in very contrasted velocity models: a massively parallel approach and its associated tools. *Geophysical Journal International*, 105(1):271–284.

Sjoeberg, T. A., Gelius, L.-J., and Lecomte, I. (2003). 2-d deconvolution of seismic image blur. *SEG Extended Abstracts*, pages 1055–1058.

Yilmaz, O. (2001). *Seismic Data Analysis*. Society of Exploration Geophysicists.